Visible imaging and spectroscopy of disruption runaway electrons in DIII-D

J. H. Yu,[1,a)] E. M. Hollmann,[1] N. Commaux,[2] N. W. Eidietis,[3] D. A. Humphreys,[3] A. N. James,[4] T. C. Jernigan,[2] and R. A. Moyer[1]
[1]*University of California, San Diego, La Jolla, California 92093-0417, USA*
[2]*Oak Ridge National Laboratory, P.O. Box 2008, Oak Ridge, Tennessee 37831, USA*
[3]*General Atomics, P.O. Box 85608, San Diego, California 92186-5608, USA*
[4]*Lawrence Livermore National Laboratory, 7000 East Avenue, Livermore, California 94550, USA*

(Received 21 January 2013; accepted 28 March 2013; published online 15 April 2013)

The first visible light images of synchrotron emission from disruption runaway electrons are presented. The forward-detected continuum radiation from runaways is identified as synchrotron emission by comparing two survey spectrometers and two visible fast cameras viewing in opposite toroidal directions. Analysis of the elongation of 2D synchrotron images of oval-shaped runaway beams indicates that the velocity pitch angle $v_\perp/v_{||}$ ranges from 0.1 to 0.2 for the detected electrons, with energies above 25 MeV. Analysis of synchrotron intensity from a camera indicates that the tail of the runaway energy distribution reaches energies up to 60 MeV, which agrees with 0D modeling of electron acceleration in the toroidal electric field generated during the current quench. A visible spectrometer provides an independent estimate of the upper limit of runaway electron energy which is roughly consistent with energy determined from camera data. Synchrotron spectra reveal that approximately 1% of the total post-thermal quench plasma current is carried by the detected high-energy runaway population with energies in the range of 25–60 MeV; the bulk of the plasma current thus appears to be carried by relativistic electrons with energy less than 25 MeV. In addition to stable oval shapes, runaway beams with other shapes and internal structure are sometimes observed. © *2013 AIP Publishing LLC* [http://dx.doi.org/10.1063/1.4801738]

I. INTRODUCTION

Electrons are effectively collisionless beyond a critical energy; and thus, any finite toroidal electric field in a tokamak can accelerate these "runaway electrons" (REs) to relativistic energies. Studying REs is important because in ITER the runaway energy may be on the order of hundreds of MeV with mega amps of current, leading to serious concerns regarding possible damage to first wall components when runaways strike the vessel.[1] Runaways generated during disruptions are of particular concern because of the large electric fields that can be generated that can lead to significant runaway current. Thus, efforts are being made to develop methods to reduce the energy and current carried by runaways during disruptions in future tokamaks.

In addition to the potentially negative consequences of runaways interacting and damaging material surfaces, runaways can be used as a tool to study magnetic turbulence in the core of a tokamak plasma.[2–4] REs are also interesting in terms of fundamental physics including electron-positron pair production,[5] electron acceleration in solar flares,[6] and electrical breakdown of lightning in thunderstorms.[7]

REs have been studied previously on a number of tokamaks.[8] Imaging in particular was a key diagnostic in the following cases: during massive gas injection (MGI) experiments using IR synchrotron emission at TEXTOR,[9,10] during plasma startup using visible synchrotron emission at EAST,[11] and during disruptions using soft x-ray (SXR) tomography at JET[12] and using visible emission at HL-2A.[13] Here, we present the first visible light images of synchrotron emission from REs generated during Ar pellet-induced disruptions in DIII-D,[14] and we show visible spectra during the RE current plateau. Following previous IR imaging work on REs, we use the 2D profile and intensity of the measured synchrotron emission to infer RE properties. These include electron velocity pitch angle and the upper energy of the detected runaways, as the signal is dominated by the fastest electrons.

The paper is organized as follows: in Sec. II, the experimental setup and diagnostics are presented; in Sec. III, the generation and evolution of pellet-induced disruption REs are described; in Sec. IV, the camera spectral response and RE synchrotron spectra are shown; in Sec. V, the energy of the detected REs is obtained using spectrometer and camera data that is compared to a simple acceleration model using the 0D toroidal electric field; in Sec. VI, fast camera images are presented, which show a variety of RE beam shapes and which show forward and backward views during a shot with D_2 pellet injection; and in Sec. VII, the pitch angle is inferred from the elongation of oval shaped RE beams. We conclude with a discussion in Sec. VIII.

II. EXPERIMENTAL SETUP

REs are studied in DIII-D[14] in high confinement mode (H-mode) plasmas with both Lower Single Null (LSN) and Inner Wall Limited (IWL) configurations, with the following parameters: plasma current $I_p = 1.5$ MA, central electron temperature $T_e = 3$ keV, central electron density $n_e = 8 \times 10^{13}$ cm^{-3}, 2–6 MW of neutral beam heating, and toroidal magnetic field $B_T = 2.1$ T. The plasma is rapidly shut down by injecting a 2.7 mm diameter cryogenic Ar pellet

a)e-mail: jyu@ferp.ucsd.edu

from the outboard midplane of the vessel aimed roughly at the magnetic axis with velocity approximately 500 m/s. More detailed discussion of rapid shutdown experiments in DIII-D can be found in Refs. 15 and 16. We find Ar pellet shutdown of IWL plasmas with nearly circular cross section produces significant RE current 4× more reliably than LSN target plasmas (approximately 80% success rate for IWL vs. 20% for LSN).[17,18] This suggests that seed REs are deconfined in LSN plasmas more readily than in IWL plasmas possibly due to strong MHD activity during the thermal quench. In addition to plasma shape, the method of plasma shutdown is an important factor in determining the peak RE current in DIII-D. This is consistent with previous work showing cryogenic pellet injection[19] generates larger RE current compared to gas injection.

Two CMOS fast cameras (a 12-bit Phantom v7.1 and a 14-bit Phantom v7.3) sensitive to wavelengths in the range of ~450–950 nm and framing at ~24,000 frames per second (fps), are used to study the RE evolution. More information on these cameras can be found in Ref. 20. One camera detects RE synchrotron radiation by looking toward the direction of electron approach (forward-viewing) with one of the following optical filters: a long-pass (>700 nm) filter; a narrowband filter (bandwidth 15 nm) with central wavelength at 747 nm which is in a line-free region of the spectrum; a narrowband filter (bandwidth 10 nm) at 912 nm; and no filter. As shown by the shaded camera regions in Fig. 1, a second camera is used to view in the opposite direction as electron approach (backward direction) with one of the following filters: a D_α filter at 656 nm; an Ar I filter at 697 nm; an Ar II filter at 611 nm; and no filter. The lines of sight for the forward and backward viewing spectrometers are also shown in Fig. 1, along with the Ar pellet trajectory and the directions of the toroidal magnetic field, RE motion, plasma current, and plasma rotation.

In addition to fast visible cameras, a suite of diagnostics is used during the rapid plasma shutdown and RE evolution, including single-chord visible and ultraviolet survey spectrometers, soft x-ray poloidal arrays for fast radiated power, a four-chord CO_2 interferometer for electron density measurements, and magnetic loops. A hard x-ray (HXR)/gamma scintillator array, consisting of 12 barium-germanium-oxide (BGO) scintillators placed around the machine outside the vacuum vessel at 6 toroidal locations and 3 poloidal locations, is used to detected the time and approximate spatial location of REs hitting the wall.[21]

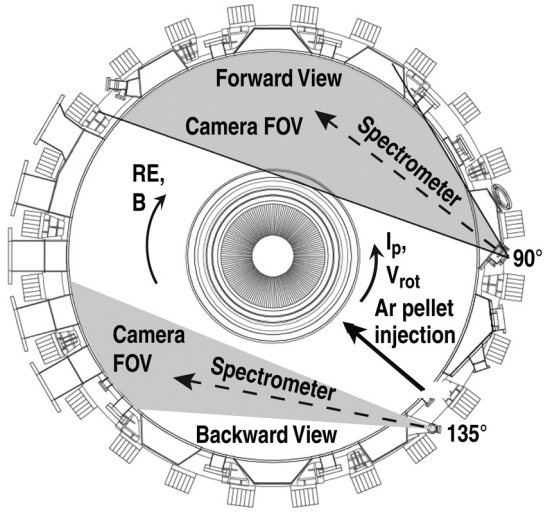

FIG. 1. Top view of the DIII-D tokamak showing the Ar pellet trajectory. The shaded regions show the FOV for the two opposite viewing cameras, and the dashed lines show the spectrometer views. The runaway motion and magnetic field are in the clockwise direction.

III. GENERATION AND EVOLUTION OF REs DURING PELLET-INDUCED PLASMA SHUTDOWN

A sufficiently large Ar pellet (2.7 mm diameter used for the present study) injected into a stable plasma initiates the plasma shutdown. A radiative cooling front is created by the pellet ablation, and when this pressure perturbation reaches the $q = 2$ surface, unstable MHD activity is triggered and the plasma temperature suddenly drops on a timescale of a few tens of microseconds, known as the thermal quench (TQ). In pellet-induced disruptions that have appreciable RE current (>50 kA), a non-thermal electron cyclotron emission (ECE) spike is seen immediately following the TQ. After the loss of plasma thermal energy, the increased resistivity in the cold plasma causes the plasma current to decrease (known as the current quench CQ) on a timescale set by the plasma inductance. During the CQ, this non-thermal ECE signal is believed to indicate the presence of confined fast electrons, suggesting prompt RE formation during the TQ. The HXR detector also detects a prompt loss of RE to the wall; this prompt loss is thought to be REs that are generated during the TQ and born on stochastic field lines and thus lost rapidly, as predicted by NIMROD simulations[22] of diverted plasmas. NIMROD simulations of limited plasmas not only had minimal stochasticity but also showed early runaway loss (although less than diverted plasmas). The shot-to-shot variation in detected peak RE current at later times is possibly due to subtle variations in the magnitude and confinement of the RE seed population. At these early times in the plasma shutdown (within a few ms of the Ar pellet injection), the light detected in unfiltered camera images is dominated by Ar line radiation.

The confined, on-axis, REs are accelerated by the loop voltage[23] generated during the CQ, converting up to 50% of pre-disruption plasma current into RE current. Figure 2(a) shows time traces of the plasma current, a soft x-ray signal from a sightline viewing near tangential to the center of the vessel, and the spatially integrated camera signal from the forward viewing camera.

An interesting scenario unfolds during the RE plateau phase in which the REs carry nearly all the current and sustain a cold background plasma that has ~100× the RE density. Approximately 6 ms after the pellet is injected into the plasma, the camera detects a roughly circular profile of synchrotron emission from REs near the center of the vessel. REs are actually formed before this time, as early as the TQ, but the visible camera is sensitive to REs with energy greater than ~25 MeV due to the sharp cutoff of synchrotron emission at short wavelengths. It takes time for both the number and energy of the runaways to increase to a detectable visible

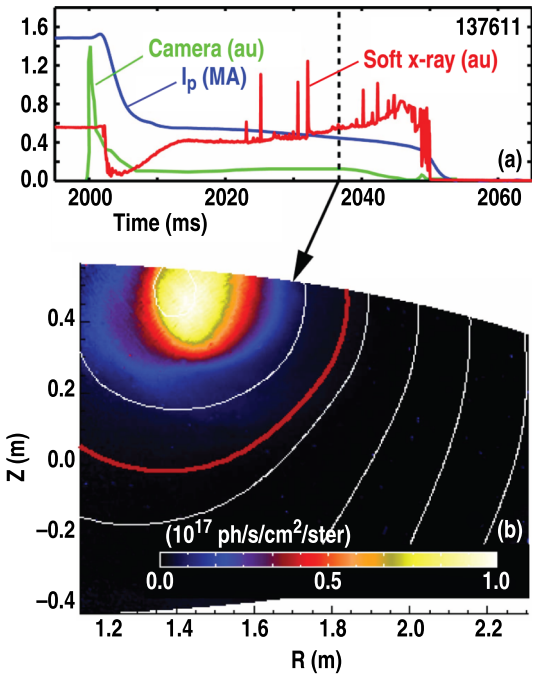

FIG. 2. (a) Time traces of plasma current (blue), a soft x-ray channel (red), and the spatially integrated camera signal (green). (b) Synchrotron emission from REs detected in broad-band visible light (no filter) from the forward viewing camera, with reconstructed flux surfaces overlaid. The thick red curve shows the last closed flux surface.

signal. Figure 2(b) shows an image of synchrotron emission from the forward viewing camera during the runaway current plateau; overlaid on the figure are JFIT[24] contours of normalized minor radius ρ mapped to the point of tangency for each pixel's sightline, with the last closed flux surface shown in red. The RE beam location agrees with the reconstructed flux surface contours.

For the shot shown in Fig. 2, the visible emission profile of the RE beam is initially ~25 cm in radius and narrows with time. Just before the RE beam hits the wall the RE beam radius is ~10 cm, which occurs in this shot about 50 ms after the pellet injection. The narrowing of the detected emission profile could be due to loss of edge REs due to loss to the wall. The narrowing of the RE visible emission could also indicate that the RE energy profile becomes more peaked, as emission from only the highest energy electrons are detected in the visible spectral range. Interestingly, early work[25] predicts a decrease in runaway beam radius due to $\bar{E} \times \bar{B}$ drifts of runaway electrons.

Confinement of the RE beam has been accomplished using the plasma control system (PCS) to prevent the vertical instabilities. The runaway lifetime up to the volt-second limit of the ohmic coil (>600 ms) has been achieved (prior to using the PCS system, most of the RE beams were lost due to vertical drift with a maximum lifetime of ~50 ms). Robust linear position estimators allow vertical control of the RE beam, and the RE beam current is controlled using ohmic coil feedback. Using the PCS control, the RE current has been ramped down to zero in a controlled fashion.[26] At the end of the runaway control phase, the RE beam typically drifts radially inward toward the vessel centerpost. When the runaway beams make contact with the wall a "dust shower" consisting of hundreds of small pieces of eroded wall material is often observed.

IV. SYNCHROTRON SPECTRA OF RUNAWAYS

Here, we briefly overview the spectral characteristics of synchrotron radiation. The synchrotron spectral power density $dP/d\lambda$ emitted by a relativistic electron was derived in Ref. 27 using the Schwinger approach.[28] For relativistic electron motion in a tokamak including toroidal motion, gyromotion, and vertical centrifugal drift, $dP/d\lambda$ takes the approximate form,[29]

$$\frac{dP}{d\lambda}(\lambda,\theta,\gamma) \approx 10^{-9}\frac{\pi m_o c^2 r_e}{h}\sqrt{\frac{2\sqrt{1+\eta^2}}{\gamma\lambda^3 R_o}} \times \left(I_o(\zeta)+\frac{4\eta}{1+\eta^2}I_1(\zeta)\right)\exp\left(-\frac{4\pi R_o}{3\lambda\gamma^3\sqrt{1+\eta^2}}\right), \quad (1)$$

where the effect of gyromotion on the curvature of the RE trajectory is in the term $\eta \equiv eB\theta R_o/m_o c\gamma$, I_o, and I_1 are modified Bessel functions, r_e is the classical electron radius, h is Planck's constant, c is the speed of light, and $\zeta \equiv 4\pi R_o\eta/3\lambda\gamma^3(1+\eta^2)^{3/2}$. All input quantities are expressed in SI units, and $dP/d\lambda$ has units of photons/s/nm. Equation (1) is valid for wavelengths smaller than the peak wavelength of the synchrotron emission, which is in the IR for RE energies in present day tokamaks. $dP/d\lambda$ depends on the RE energy ε (characterized by γ) and on the radius of curvature, which in turn depends on the average major radius R_o of the electron trajectory and velocity pitch angle $\theta = v_\perp/v_{||}$. The electron kinetic energy ε is related to the relativistic factor via $\gamma = 1 + \varepsilon/m_o c^2$, where $m_o c^2 = 0.511$ MeV is the rest mass of an electron.

Figure 3 shows the spectral power of synchrotron emission from a single relativistic electron for relevant DIII-D parameters over a range of energies and for two pitch angles, shown as the solid and dashed lines. Synchrotron emission peaks in the IR for tokamak runaways, and higher RE energy shifts the peak synchrotron emission toward the visible region of the spectrum. The strong dependence of $dP/d\lambda$ on γ makes

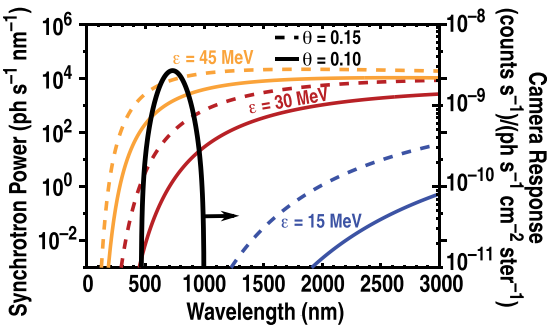

FIG. 3. Synchrotron spectral curves for three chosen RE energies of 15 MeV (blue), 30 MeV (red), and 45 MeV (orange). At each energy, the synchrotron spectrum is shown for electron velocity pitch angle $\theta = 0.10$ (solid) and 0.15 (dashed). The unfiltered camera system response is shown as the black solid line.

synchrotron radiation an excellent diagnostic of electron energy; however, the strong dependence also means that the highest energy electrons dominate the visible signal, so only the tail of the distribution is detected. The black line in Fig. 3 shows the camera system's response, which is obtained from a Gaussian fit to calibrated intensity measurements using narrowband interference filters spanning the visible spectral region. The steep cutoff of synchrotron emission at short wavelengths makes the visible camera insensitive to runaways with energy less than approximately 25 MeV.

The brightness of the measured synchrotron radiation depends on the number of observed REs N_{obs}, electron pitch angle θ, and RE energy ε. In Sec. V, runaway parameters are determined by comparing the brightness expected from a RE beam to intensity-calibrated spectrometer and camera measurements. The brightness of a runaway beam is given by

$$B = \frac{dP}{d\lambda}\frac{N_{obs}}{A_{spot}\Omega_d},$$

where A_{spot} is the area of the detector element projected onto the RE beam, and $\Omega_d = A_d/s^2$ is the solid angle subtended by the detector optics with collection area A_d located a distance s away from the detected RE beam. Due to the forward-beaming nature of runaways, only a toroidal fraction $\approx 2\theta/2\pi$ of the runaways contribute to the measured signal at any given time. In addition, the finite size of collection optics limits the number of photons detected. Taking these effects into consideration leads to a brightness that can be expressed as (units of photons/s/m^2/nm/ster),

$$B(\lambda, \theta, \varepsilon) = \frac{dP}{d\lambda}\frac{2R_o}{\pi\theta}n, \quad (2)$$

where n is the density of observed REs. Equation (2) allows us to relate the theoretical spectral emission $dP/d\lambda$ from a single RE to the expected brightness in a tokamak, which can then be compared to measured brightness. The estimate in Eq. (2) is for highly relativistic electrons with $1/\gamma \ll \theta$. In addition, the visible signal from bremsstrahlung emission due to runaways scattering off cold background ions has been estimated and is negligible for the conditions studied here. The analysis based on Eq. (2) allows the runaway electron energy and density to be determined from the measured spectrum if the pitch angle is known. Here, the pitch angle θ is obtained from the shape of the runaway beams as measured by the forward viewing camera and is described in Sec. VII, with typical values for θ ranging from 0.1 to 0.2 for all oval-shaped runaway beams. We have analyzed the statistical uncertainty in the fitting procedure used in determining θ for individual shots and find that the typical standard deviation is $\Delta\theta = \pm 0.02$. Since the synchrotron brightness depends on pitch angle, $\Delta\theta$ produces an uncertainty in the runaway energy of $+4$ MeV and -2 MeV. However, the error in our determination of the runaway energy is dominated by the uncertainty in the intensity calibration of the spectrometers and camera. Using a calibration uncertainty of a factor of 2, the uncertainty in the runaway energy is approximately $+15$ MeV and -10 MeV.

Note that comparing spectroscopic and imaging data to Eq. (2) provides no detailed information on the energy distribution of runaways, which is modeled in this paper as monoenergetic. The analysis is not very sensitive to the exact shape of the modeled energy distribution function, because the highest energy electrons dominate the synchrotron signal due to the sharp cutoff of the synchrotron spectrum at short wavelengths. Previous work has shown that the inferred energy changes by $<15\%$ when the assumed distribution is changed from monoenergetic to flat.[30]

V. ENERGY OF RUNAWAYS

A. Visible spectra during the RE plateau

Two intensity-calibrated visible survey spectrometers view the plasma in opposite toroidal directions and are used to identify the spectrum of emission detected by the cameras. We find that the forward detected visible spectrum during the RE current plateau is dominated by synchrotron emission from runaways. The spectrometers view the plasma through the same ports as the forward and backward viewing cameras, with an integration time of 15 ms and with a viewing spot size of approximately 1 cm diameter aimed at the center of the vessel. Figure 4 shows the backward and forward detected spectra (respectively) during the runaway current plateau. Both spectra contain multiple lines including D_α,

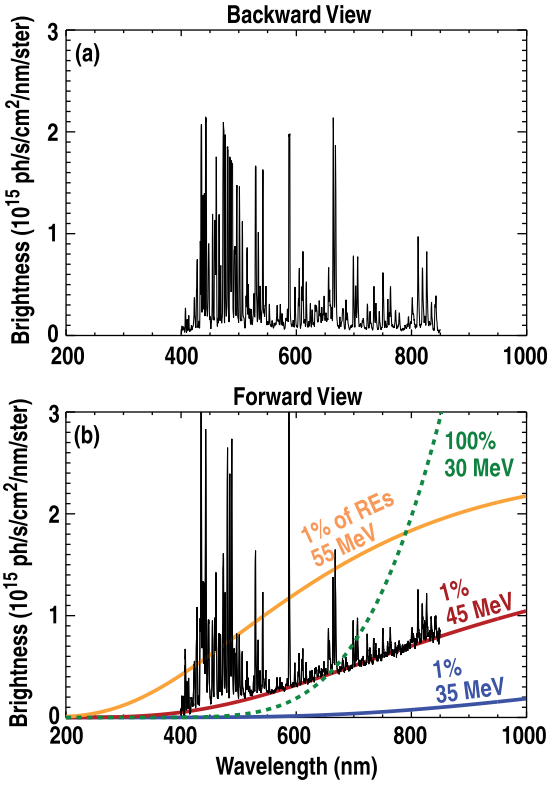

FIG. 4. (a) Backward and (b) forward detected survey spectra during the runaway plateau at $t = 2080$ ms in shot 145524. (b) Solid curves show the calculated synchrotron brightness for RE energies of 35 MeV (blue), 45 MeV (red), and 55 MeV (orange), with detected REs carrying 1% of the total measured current. The dashed green curve shows the synchrotron spectrum with detected REs carrying 100% of the measured current and with energy of 30 MeV. The red curve gives the best fit to the shape and magnitude of the measured continuum spectrum.

D_β, CIII, and Xe lines due to weak Xe gas injection during the runaway current plateau. What is striking in these spectra is the difference between the continuum signals in the forward and backward detected data. The forward detected continuum signal is much larger than the backward signal, and the forward continuum signal increases with wavelength as expected for synchrotron radiation.

The predicted synchrotron brightness from Eq. (2) for monoenergetic electron distributions is shown in Fig. 4(b) using a pitch angle of $\theta = 0.15$, which is determined from the shape of the oval synchrotron emission detected by the camera. An excellent match to the forward data is obtained using a runaway energy of 45 MeV with the detected runaways carrying approximately 1% of the total measured current. This small fraction of the total current is determined from the spectral shape of the measured continuum radiation. That is, the predicted brightness matches the data using a density that is only 1% of the total inferred runaway density $n_{re} = I_p/(ecA_{re}) \approx 10^{10} - 10^{11}\,\mathrm{cm}^{-3}$, where I_p is the plasma current measured with Rogowski loops and A_{re} is the cross-sectional area of the runaway beam. If all the current is assumed to be contributing to the measured visible signal, the shape of the calculated synchrotron signal cannot be matched to the data for any runaway energy, as shown by the dashed line in Fig. 4(b). Thus, analysis of the forward detected visible spectrum reveals that the majority of the runaways have a smaller energy than the cutoff energy for visible synchrotron detection, which is ~25 MeV.

The forward viewing spectrometer typically detects a decrease in the brightness of the impurity lines and an increase in the continuum radiation toward the end of the runaway plateau. This is consistent with an increase in brightness toward the end of the shot measured with the forward viewing camera, and supports our contention that the forward viewing camera images are dominated by synchrotron emission (rather than line radiation) during the runaway plateau.

B. Camera synchrotron imaging and simple model of runaway acceleration

Similar to the analysis of the spectral data, we also infer the upper energy of the RE population using the synchrotron brightness detected by a calibrated camera. The measured signal S from the RE beam can be expressed as

$$S = \int B(\lambda, \theta, \varepsilon) F(\lambda) d\lambda, \tag{3}$$

where the camera spectral response $F(\lambda)$ includes the effects of interference filters if used, and $B(\lambda, \theta, \varepsilon)$ is calculated from Eq. (2). This forward-modeled signal is compared with the intensity of the actual camera signal S_{cam} for a range of RE energies, assuming a monoenergetic distribution. The inferred RE energy is the modeled signal that matches the measured signal, i.e., the energy that satisfies the condition $S = S_{cam}$.

Figure 5(a) shows the evolution of the plasma current I_p following the disruption induced by Ar pellet injection at $t = 2000$ ms, and the electric field is shown in Fig. 5(b). The results of camera synchrotron analysis are shown in Fig. 5(c). The energy data points are calculated assuming 1% of the current is carried by the high-energy electrons, revealing that the fastest runaways reach energy of approximately 60 MeV in this shot (137611). The error bars are determined by allowing a factor of two in the uncertainty of the camera calibration.

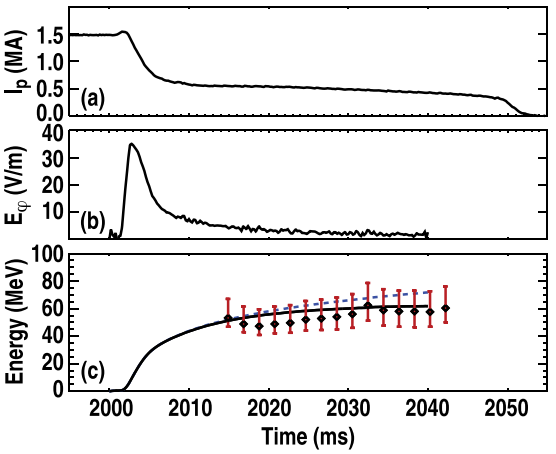

FIG. 5. The evolution of (a) plasma current, (b) toroidal electric field, and (c) RE energy obtained from a 0D model with synchrotron loss (solid) and no synchrotron loss (dashed) for shot 137611. The energy data points (black dots) are obtained from the synchrotron emission detected by the forward viewing camera with no filter.

The inferred energy of the fastest runaways is compared to a simple model of electron acceleration in the toroidal electric field created during plasma shutdown. The loop voltage V_l is calculated at each time step and the toroidal electric field E is obtained. The rate of change of electron energy is given by the power imparted to the electron from the electric field, with power loss due to synchrotron emission. The predicted electron energy ε is found by integrating $(d\varepsilon/dt) = P_E - P_s$, where the electric field power is given by $P_E = ecE = (ecV_l/2\pi R_o)$ and the synchrotron loss is $P_s = (2m_o c^3 r_e \gamma^4/3R_c^2)$. The electron cyclotron radius R_c is approximated in Ref. 31 as $(1/R_c) \approx (1 - \theta^2/R_o) + (eB\theta/\gamma m_o c)$, where the first term describes the toroidal motion of the guiding center, and the second term is due to gyromotion. The loop voltage is given by $V_l = [(M^2/L_w) - L_p]\,(dI_p/dt) + I_w R_w (M/L_w)$, where the current I_w through the vessel wall is determined from the difference between the current measured with Rogowski loops outside the vessel and the current measured with magnetic probes inside the vessel, and R_w is the wall resistivity. The mutual inductance M between the plasma and the vessel wall, the plasma inductance L_p, and the wall inductance L_w are calculated during the runaway channel using a finite element eigenmode representation in the TokSys code.[32] The model of electron acceleration with and without the synchrotron loss term is shown in Fig. 5(c) as the solid and dashed lines, respectively. With no synchrotron loss term, the model predicts the unphysical result of RE energy increasing indefinitely with any finite electric field. However, it is seen that the data matches the 0D model reasonably well when synchrotron loss is included, indicating that the seed population of

electrons is accelerated in a toroidal electric field on the order of a few tens of V/m during the current quench, and that maximum RE energy reaches approximately 60 MeV in this case.

VI. RUNAWAY IMAGES IN THE VISIBLE SPECTRAL REGION

Runaways have been imaged using a variety of diagnostic imaging configurations with two cameras sometimes running simultaneously, with and without interference filters, and with both cameras forward-viewing as well as viewing in opposite toroidal directions. The 2D synchrotron images show that the RE beam usually forms in a roughly circular shape. However, a number of other interesting shapes and structures are sometimes observed. Note that the actual shape of the RE beam may not be the same as the shape of the forward detected emission, because the forward beaming nature of synchrotron radiation from relativistic electrons means that the electron trajectory (and not just the volumetric toroidal "tube" of runaways) is an important factor in determining the detected shape of the beam. For example, a circular RE beam appears as a tilted ellipse when viewed in the direction of electron approach due to the finite angle of emitted radiation and due to field line helicity (more details are in Sec. VII).

Figure 6 shows an example of a forward detected synchrotron image that has a crescent shape, with the visible synchrotron intensity much higher on the high field side (inner wall located at R=1 m) compared to the low field side of the plasma. Other shots have a thinner crescent shape with a nearly annular radiation pattern. This shape can persist for hundreds of milliseconds and requires more investigation to understand its origin. A similar shape was observed in visible light for startup runaways in EAST.[11] In shot 146704 shown in Fig. 6, an unknown instability (which occurs after the time shown in the figure) causes the crescent to suddenly change to an oval shape on a timescale of approximately 100 μs. This sudden change in the synchrotron radiation is accompanied by a transient high flux of gamma rays, presumably due to some fraction of the runaways hitting the wall. The cause of the crescent emission is unknown at present but could be due to runaways scattering off cold background plasma or neutrals at large minor radius, leading to runaways with a large pitch angle ($\theta \approx 1$) and strong emission.

In other shots, there appears to be two runaway beams shortly following the Ar pellet injection (within 5 ms) with spatial dimension of a few centimeters as shown in Fig. 7. The pair of beams typically drifts radially outward on a timescale of a few milliseconds. In this shot and in others with a small pair of beams, no RE plateau forms. It is possible that the drift of these small beams and subsequent contact with the wall are responsible for the loss of the seed runaway population. However, these small beams are only occasionally observed when there is no current plateau.

In some long-lived runaway beams, 2D structure can be seen in the synchrotron emission pattern, and this pattern is sometimes observed to suddenly rotate (less than one poloidal revolution) possibly due to changes in magnetic island topology. Following this partial rotation or shift, the radiation pattern becomes stationary again. In other shots, periodic rotation of internal structure in the RE beam is observed, similar to RE snakes reported in Refs. 3 and 33.

We next focus on a shot with D_2 pellet injection during the RE plateau in which two fast cameras view in opposite toroidal directions. The images in Fig. 8 are from the two cameras at three times during the RE current plateau, with Figs. 8(a)–8(c) showing the backward view and Figs. 8(d)–8(f) showing the forward view. The images show a striking difference in emission patterns in the opposing toroidal views. The backward viewing camera is unfiltered and detects radiation from 450 to 950 nm with radiation sources mainly consisting of D, Ar, and C. The intensity in Fig. 8(a) has been increased by a factor of 2.5 for visibility. The forward viewing camera has a 912 nm filter with bandwidth of 10 nm and detects synchrotron radiation from high energy runaways. A cryogenic D_2 pellet is injected into the RE beam at t = 2028 ms in order to study collisional suppression of runaways. The synchrotron emission is not affected by the D_2 pellet injection as shown in Fig. 8(e), either because the pellet is ablated by runaways with energy lower than the cutoff for visible synchrotron detection, or because the highly relativistic electrons are simply not affected by deuterium

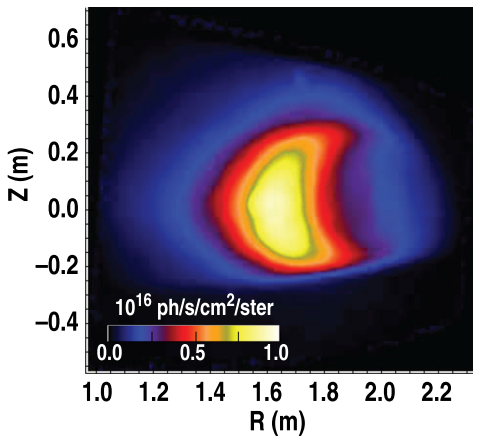

FIG. 6. Crescent-shaped RE beam observed in shot 146704 at t = 2175 ms with a 747 nm filter. Inner wall radius is located at R = 1.0 m.

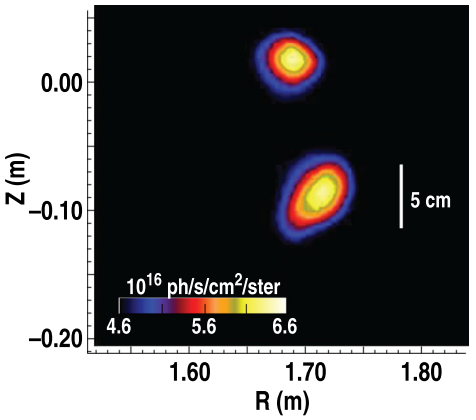

FIG. 7. A pair of small RE beams detected by the forward viewing camera in shot 142729 at t = 2005 ms using a filter that passes long wavelengths (>700 nm). The color scale has been adjusted to maximize visibility, with black corresponding to finite radiance rather than zero radiance.

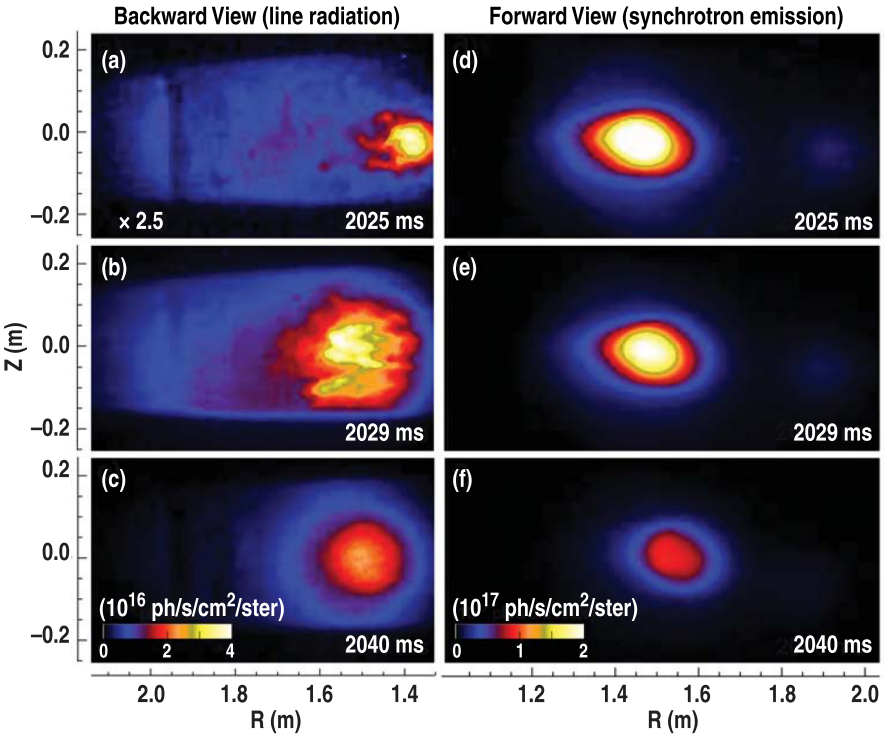

FIG. 8. Backward (a)–(c) and forward (d)–(f) viewing camera images during the RE current plateau in shot 142725. The backward viewing camera detects broadband light and the forward detected camera has a narrowband filter with central wavelength at 912 nm and bandwidth of 10 nm. A fragmented deuterium pellet was injected into the runaway beam at time $t = 2028$ ms, just before the time corresponding to images (b) and (e).

ions which reach the core of the RE beam. In contrast, the backward viewing camera images reveal a rapidly evolving, complex filamentary spatial pattern of line emission due to turbulence following the pellet injection, presumably due to runaways interacting with impurity and D_2 gas near the edge of the runaway beam. For this case of D_2 pellet injection (and for a separate case of He gas injection), no significant decrease of RE current is observed. However, there is a decrease of runaway current due to high-Z impurity injection, and these results will be presented elsewhere.

A difference is seen in the shapes of the emission patterns from opposing camera views, with an ellipse seen in the forward images and a circle seen in the backward detected images. The circular backward detected image in Fig. 8(c) shows brightness extending to larger minor radii than the synchrotron image in Fig. 8(f). The circular emission pattern seen in the backward detected image is due to runaways exciting D and impurity gas and indicates the actual 2D radius of the runaway beam, while the smaller pattern detected by the forward viewing camera is due to the fact that the synchrotron radiation at 912 nm is due only to the high-energy tail of the runaway population. Rough reconstructions of the RE beam radial profile using soft x-ray and interferometer measurements indicate that the RE beam current is dominantly concentrated in a narrow beam but is surrounded by a larger diffuse RE halo. This can also be seen in the backward detected images. The forward detected images have an elliptical shape due to the forward-beaming nature of relativistic synchrotron radiation in combination with the finite velocity pitch angle of the electrons, as discussed in Sec. VII.

VII. PITCH ANGLE

Here, we infer the RE trajectory based on the elongation of the 2D synchrotron emission, with the analysis restricted to oval-shaped runaway beams. Some elongation of the RE beam can be due to the drift orbit shift of different energy electrons within the beam,[34] but because the visible camera signal is dominated by the fastest electrons and thus restricted to a relatively narrow energy range, the observed elongation is attributed to the pitch angle θ.[29,35]

For relativistic electrons, the radiation from each electron is emitted into a cone where the angle of emission depends on the electron energy and perpendicular momentum, with full opening angle $\alpha = 2\theta + 1/\gamma \approx 2\theta$, where $\theta = v_\perp/v_{||}$. The term $1/\gamma$ can be neglected because it is approximately an order of magnitude smaller than the experimentally inferred value of θ. Thus, for highly relativistic electrons the opening angle of the forward-directed synchrotron radiation is strongly determined by the cyclotron motion. We follow previous analysis[29,30] to infer the divergence of the radiation and thus θ. Due to toroidal curvature of the electron orbit and finite opening angle α for the cone of forward radiation, the camera's tangential view of a circular RE beam detects a larger horizontal extent of radiation compared to the vertical extent by the amount $\Delta r = R_o(1 - \cos\theta) \approx R_o\theta^2$, as shown in Fig. 9. This results in an elliptical shape of the detected radiation. Helical field lines create a tilted ellipse because on the high field side of the magnetic axis REs travel upward toward the forward viewing camera, while on the low field side REs travel slightly downward. For a circular cross section runaway beam, this field line effect in combination with finite θ results in a forward-measured 2D radiation spatial profile that is a tilted ellipse with respect to the equatorial plane.

To determine the pitch angle, the RE beam is fit with an ellipse using an intensity contour that is chosen to be 50% of the maximum intensity. The result of such a fit is shown in Fig. 10 as the dashed oval with major axis $a = 16$ cm and minor axis $b = 11$ cm. The pitch is calculated as $\theta = \sqrt{(a-b)/R_o}$ yielding a pitch angle for this case of

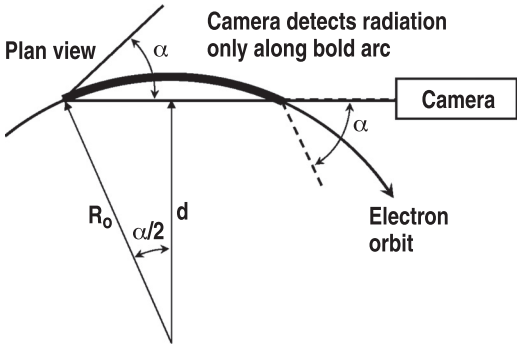

FIG. 9. Top-view schematic showing the horizontal extension of detected radiation from a relativistic electron with angle of emission α. The electron guiding center moves in a circular orbit with major radius R_o. For a circular beam, the horizontal dimension of detected radiation exceeds the vertical dimension by the amount $\Delta r = R_o - d = R_o - R_o \cos(\alpha/2)$. Adapted from Ref. 30.

approximately 0.17. We find values for θ for oval shaped runaway beams typically range from 0.10 to 0.20, which are similar in magnitude with those inferred for startup REs in TEXTOR.[29]

VIII. DISCUSSION AND SUMMARY

The fastest REs have energy that is roughly consistent with acceleration due to the 0D toroidal electric field induced during the current quench, although the source of the RE seed term is currently unknown. While the energy determined from the synchrotron intensity matches the 0D model quite well, it is uncertain whether the synchrotron loss is the only mechanism limiting the runaway energy. Other loss mechanisms may be important such as resonance between the electron gyromotion and magnetic error fields in DIII-D.

The difference in size, shape, and intensity of the images from the forward and backward viewing cameras indicate several things: (i) there is an energy profile to the RE beam, (ii) the shape of the forward emission is affected by the radiation cone angle, and (iii) different physical mechanisms generate the radiation detected in the opposing views. The runaways detected by the forward viewing camera in visible synchrotron light are limited to highly relativistic electrons

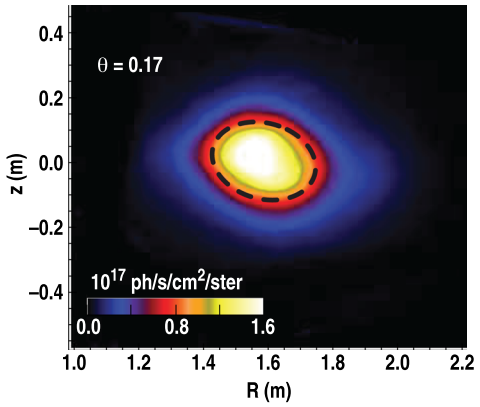

FIG. 10. Forward detected camera image from shot 142726 at $t = 2030$ ms using a narrowband filter with central wavelength 912 nm. The black dashed oval is the result of fitting an ellipse to the 50% intensity contour; the major and minor axes of the ellipse-fit are used to determine the runaway pitch angle.

with energy greater than 25 MeV. The emission detected at larger radii in the backward data is attributed to a diffuse halo of lower energy runaways that excite background plasma. The radial variation in energy could be due to a stronger resonance between runaways and the magnetic field ripple at the edge of the beam, which would result in a larger pitch angle and thus a stronger radiative loss.[36]

The relatively large values of θ are consistent with theoretical predications of avalanche creation of relativistic electrons, because during avalanching the transverse momentum is predicted to be significant.[37,38] Avalanching is also supported by our determination that the fastest electrons detected in the visible spectrum do not carry much of the current, since avalanching would result in a broad distribution function. However, it is not known yet if avalanching occurs in DIII-D and the physics behind the formation of the runaway seed population is still being investigated. In addition to understanding the generation mechanism of the RE beam during disruptions, future work includes studying the variety of instabilities and detected shapes of the RE beam, and possibly inferring details of the magnetic topology based on runaway images.

In conclusion, we present the first visible-light images of disruption-generated runaway electrons, and show that the forward viewing camera detects synchrotron radiation from high energy electrons that have energy up to 60 MeV. Synchrotron emission measured by both the visible spectrometer and the visible camera is dominated by the high-energy electron population because of the sharp cutoff of synchrotron emission at short wavelengths. Fitting the magnitude and shape of the forward detected spectroscopic data to synchrotron spectra reveals that approximately 1% of the measured current is carried by high energy runaways with approximate energy of 45 MeV. The camera-measured oval shape of the synchrotron runaway beam is used to determine the pitch angle $\theta = v_\perp/v_{||}$ of runaways, which ranges from 0.1 to 0.2. The analysis presented here is done on RE beams with oval shapes, however, other shapes are sometimes observed. As expected for relativistic electrons emitting synchrotron emission, a striking difference in the shape and intensity of the emission is seen in the forward versus backward viewing cameras. The high energy RE population is unaffected by deuterium pellet injection and by low-Z gas injection. High-Z impurity injection may be a possible means to collisionally suppress runaways in order to avoid wall damage in future fusion devices, and this will be addressed in a future paper.

ACKNOWLEDGMENTS

The authors would like to thank M.A. Van Zeeland, N. Brooks, A. McLean, and C. Tsui for useful discussions and spectroscopic support. This work was supported by the U.S. Department of Energy under DE-FG02-07ER54917, DE-AC05-00OR22725, DE-FC02-04ER54698, and DE-AC52-07NA27344.

[1]R. Nygren, T. Lutz, D. Walsh, G. Martin, M. Chatelier, T. Loarer, and D. Guilhem, J. Nucl. Mater. **241–243**, 522 (1997).
[2]H. Dreicer, Phys. Rev. **115**, 238 (1959).

[3]R. Jaspers, N. J. Lopes Cardozo, K. H. Finken, B. C. Schokker, G. Mank, G. Fuchs, and F. C. Schüller, Phys. Rev. Lett. **72**, 4093 (1994).
[4]I. Entrop, N. J. Lopes Cardozo, R. Jaspers, and K. H. Finken, Phys. Rev. Lett. **84**, 3606 (2000).
[5]P. Helander and D. J. Ward, Phys. Rev. Lett. **90**, 135004 (2003).
[6]E. Moghaddam-Taaheri and C. K. Goertz, Astrophys. J., Part 1 **352**, 361–375 (1990).
[7]A. Gurevich, G. Milikh, and R. Roussel-Dupre, Phys. Lett. A **165**, 463 (1992).
[8]R. Yoshino and S. Tokuda, Nucl. Fusion **40**, 1293 (2000).
[9]S. A. Bozhenkov, M. Lehnen, K. H. Finken, M. W. Jakubowski, R. C. Wolf, R. Jaspers, M. Kantor, O. V. Marchuk, E. Uzgel, G. Van Wassenhove, O. Zimmermann, D. Reiter, and TEXTOR Team, Plasma Phys. Controlled Fusion **50**, 105007 (2008).
[10]K. H. Finken, J. G. Watkins, D. Rusbüldt, W. J. Corbett, K. H. Dippel, D. M. Goebel, and R. A. Moyer, Nucl. Fusion **30**, 859 (1990).
[11]Y. Shi, J. Fu, J. Li, Y. Yang, F. Wang, Y. Li, W. Zhang, B. Wan, and Z. Chen, Rev. Sci. Instrum. **81**, 033506 (2010).
[12]R. D. Gill, B. Alper, M. de Baar, T. C. Hender, M. F. Johnson, V. Riccardo, and EFDA-JET Team, Nucl. Fusion **42**, 1039 (2002).
[13]Y. P. Zhang, Yi. Liu, G. L. Yuan, M. Isobe, Z. Y. Chen, J. Cheng, X. Q. Ji, X. M. Song, J. W. Yang, X. Y. Song, X. Li, W. Deng, Y. G. Li, Y. Xu, T. F. Sun, X. T. Ding, L. W. Yan, Q. W. Yang, X. R. Duan, Y. Liu, and HL-2A Team, Phys. Plasmas **19**, 032510 (2012).
[14]J. L. Luxon, Nucl. Fusion **42**, 614 (2002).
[15]E. M. Hollmann, N. Commaux, N. W. Eidietis, T. E. Evans, D. A. Humphreys, A. N. James, T. C. Jernigan, P. B. Parks, E. J. Strait, J. C. Wesley, J. H. Yu, M. E. Austin, L. R. Baylor, N. H. Brooks, V. A. Izzo, G. L. Jackson, M. A. van Zeeland, and W. Wu, Phys. Plasmas **17**, 056117 (2010).
[16]E. M. Hollmann, P. B. Parks, D. A. Humphreys, N. H. Brooks, N. Commaux, N. Eidietis, T. E. Evans, R. Isler, A. N. James, T. C. Jernigan, J. Munoz, E. J. Strait, C. Tsui, J. Wesley, and J. H. Yu, Nucl. Fusion **51**, 103026 (2011).
[17]A. N. James, M. E. Austin, N. Commaux, N. W. Eidietis, T. E. Evans, E. M. Hollmann, D. A. Humphreys, A. W. Hyatt, V. A. Izzo, T. C. Jernigan, R. J. La Haye, P. B. Parks, E. J. Strait, G. R. Tynan, J. C. Wesley, and J. H. Yu, Nucl. Fusion **52**, 013007 (2012).
[18]R. S. Granetz, D. G. Whyte, and V. A. Izzo, Bull. Am. Phys. Soc. **54**, 231 (2009).
[19]T. E. Evans, D. G. Whyte, P. L. Taylor, A. G. Kellman, P. B. Parks, D. A. Humphreys, R. W. Harvey, S. C. Luckhardt, T. C. Jernigan, M. J. Schaffer, L. R. Baylor, A. W. Hyatt, R. L. Lee, J. A. Leuer, D. Gray, and J. Zhang, "The production and confinement of runaway electrons with impurity "Killer" pellets in DIII-D," in *Proceedings 17th IAEA Fusion Energy Conference*, Yokahama, Japan 1998 (International Atomic Energy Agency, Vienna, 1999), Vol. 3, p. 847.
[20]J. H. Yu and M. A. Van Zeeland, Rev. Sci. Instrum. **79**, 10F516 (2008).
[21]A. N. James, E. M. Hollmann, and G. R. Tynan, Rev. Sci. Instrum. **81**, 10E306 (2010).
[22]V. A. Izzo, E. M. Hollmann, A. N. James, J. H. Yu, D. A. Humphreys, L. L. Lao, P. B. Parks, P. E. Sieck, J. C. Wesley, R. S. Granetz, G. M. Olynyk, and D. G. Whyte, Nucl. Fusion **51**, 063032 (2011).
[23]M. Rosenbluth and S. Putvinski, Nucl. Fusion **37**, 1355 (1997).
[24]D. A. Humphreys and D. G. Whyte, Phys. Plasmas **7**, 4057 (2000).
[25]D. A. Spong, J. F. Clarke, and T. Kammash, Nucl. Fusion **14**, 507 (1974).
[26]N. W. Eidietis, N. Commaux, E. M. Hollmann, D. A. Humphreys, T. C. Jernigan, R. A. Moyer, E. J. Strait, M. A. Van Zeeland, J. C. Wesley, and J. H. Yu, Phys. Plasmas **19**, 056109 (2012).
[27]I. M. Pankratov, Plasma Phys. Rep. **25**, 145 (1999).
[28]J. Schwinger, Phys. Rev. **75**, 1912 (1949).
[29]R. Jaspers, N. J. Lopes Cardozo, A. J. H. Donné, H. L. M. Widdershoven, and K. H. Finken, Rev. Sci. Instrum. **72**, 466 (2001).
[30]R. Jaspers, Ph.D. dissertation (Eindhoven University of Technology, Netherlands, 1995).
[31]A. J. Russo, Nucl. Fusion **31**, 117 (1991).
[32]D. A. Humphreys, J. R. Ferron, M. Bakhtiari, J. A. Blair, Y. In, G. L. Jackson, H. Jhang, R. D. Johnson, J. S. Kim, R. J. La Haye, J. A. Leuer, B. G. Penaflor, E. Schuster, M. L. Walker, H. Wang, A. S. Welander, and D. G. Whyte, Nucl. Fusion **47**, 943 (2007).
[33]A. Weller, A. D. Cheetham, A. W. Edwards, R. D. Gill, A. Gondhalekar, R. S. Granetz, J. Snipes, and J. A. Wesson, Phys. Rev. Lett. **59**, 2303 (1987).
[34]Z. Yoshida, Nucl. Fusion **30**, 317 (1990).
[35]M. Pankratov, Plasma Phys. Rep. **22**, 535 (1996).
[36]Z. Y. Chen, B. N. Wan, Y. J. Shi, H. J. Ju, J. X. Zhu, and H. F. Liang, J. Plasma Physics **75**, 669 (2009).
[37]I. M. Pankratov, R. Jaspers, K. H. Finken, and I. Entrop, "Secondary generation of runaway electrons and its detection in tokamaks," in *Proceedings 26th EPS Conference on Controlled Fusion and Plasma Physics*, Maastricht 1999 (European Physical Society 1999), Vol. 23 J, p. 597.
[38]N. T. Besedin and I. M. Pankratov, Nucl. Fusion **26**, 807 (1986).